DTU Library

The impact of grid and spectral nudging on the variance of the near-surface wind speed

Vincent, Claire Louise; Hahmann, Andrea N.

Published in:
Journal of Applied Meteorology and Climatology

Link to article, DOI:
10.1175/JAMC-D-14-0047.1

Publication date:
2015

The DOI for this manuscript is doi: 10.1175/JAMC-D-14-0047.1

The final published version of this manuscript will replace the preliminary version at the above DOI once it is available.

If you would like to cite this EOR in a separate work, please use the following full citation:

Vincent, C., and A. Hahmann, 2015: The Impact of Grid and Spectral Nudging on the Variance of the Near-Surface Wind Speed. J. Appl. Meteor. Climatol. doi:10.1175/JAMC-D-14-0047.1, in press.

The impact of grid and spectral nudging on the variance of the near-surface wind speed

Claire Louise Vincent,*† Andrea N Hahmann

DTU Wind Energy, Technical University of Denmark, Roskilde, Denmark

*Current affiliation: The University of Melbourne, Melbourne, Victoria, Australia

†*Corresponding author address:* Claire Louise Vincent, School of Earth Sciences, The University of Melbourne, Melbourne VIC 3010, Australia

E-mail: claire.vincent@unimelb.edu.au

ABSTRACT

Grid and spectral nudging are effective ways of preventing drift from large scale weather patterns in regional climate models. However, the effect of nudging on the wind-speed variance is unclear. In this study, the impact of grid and spectral nudging on near-surface and upper boundary layer wind variance in the Weather Research and Forecasting model is analyzed.

Simulations are run on nested domains with horizontal grid spacing 15 and 5 km over the Baltic Sea region. For the 15 km domain, 36-hr simulations initialized each day are compared with 11-day simulations with either grid or spectral nudging at and above 1150 m above ground level (AGL). Nested 5 km simulations are not nudged directly, but inherit boundary conditions from the 15 km experiments.

Spatial and temporal spectra show that grid nudging causes smoothing of the wind in the 15 km domain at all wavenumbers, both at 1150 m AGL and near the surface where nudging is not applied directly, while spectral nudging mainly affects longer wavenumbers. Maps of mesoscale variance show spatial smoothing for both grid and spectral nudging, although the effect is less pronounced for spectral nudging. On the inner, 5 km domain, an indirect smoothing impact of nudging is seen up to 200 km inward from the dominant inflow boundary at 1150 m AGL, but there is minimal smoothing from the nudging near the surface, indicating that nudging an outer domain is an appropriate configuration for wind resource modelling.

1. Introduction

Simulations of the climatological wind speed distribution near the surface are a necessary part of the modeling chain for wind resource assessment. This is particularly valuable where observations are not available, or where the wind resource over a large area such as the Baltic Sea region is required for wind energy prospecting or power systems planning. Simulating the wind climate raises some of the same challenges as regional climate modeling, such as finding the optimal way of constraining the regional model to the large scale flow while allowing it to develop smaller scale variance. On the other hand, wind resource mapping demands a resolution high enough to resolve mesoscale phenomena such as topographic channelling, sea breezes and low level jets that affect the near-surface wind speed. Both the mean and distribution of the wind speed are essential because the Annual Energy Production (AEP) is a function of the wind speed distribution and the wind turbine power curve. Furthermore, understanding the variability of the wind speed across a range of time scales is required for managing the power output of the wind farm and the electricity integration into the power system. Since the variability associated with length scales of tens of kilometers is commensurate with the size of a large offshore wind farm, it can lead to large power fluctuations (e.g. Sørensen et al. 2008; Vigueras-Rodrìguez et al. 2010). The goal of this work is to explore the sensitivity of the mean and variance of the wind climate from mesoscale modeling to three methods of constraining the mesoscale model to the large scale flow.

Simulations of the regional wind climate, like all regional climate simulations, can be constrained to the large scale flow by regular and frequent initialization of the model from large scale forcing, with the first part of each model run being discarded as a 'spin-up' period, during which time the scales resolved in the simulation transition from only those in the large scale forcing, to the full effective resolution of the smaller scale model. The advantage of this method is that simulations are short enough to prevent the interior of the mesoscale model diverging from the large scale circulation patterns, but the disadvantages are wasted computational power for the spin-up period, and discontinuities between individual simulations.

Alternatively, the mesoscale simulations can be run continuously without reinitialization, but as shown by Lo et al. (2008), Bowden et al. (2012) and Bowden et al. (2013), this can result in drift from the large scale circulation patterns. It has been shown that these problems can be alleviated by nudging the regional climate model towards its difference from the large scale forcing, either by nudging in grid-point space, or by nudging in spectral space so that only wavenumbers above a certain threshold are nudged. For example, Bowden et al. (2012), Bowden et al. (2013), Liu et al. (2012), Lo et al. (2008) and Miguez-Macho et al. (2004) all showed better consistency with large scale circulation patterns in regional climate models that used nudging, although these studies were all at a horizontal resolution of 36 km or greater. Not only has nudging been shown to improve the consistency with the large scale circulation patterns, but it has also been shown to improve simulations of temperature and wind speed near the surface (Bullock et al. 2014; Bowden et al. 2012, 2013; Otte et al. 2012).

Despite the advantages of nudging in the WRF model, there is a risk that some of the variability in the regional climate model will be damped by the nudging. For example, Bowden et al. (2012) suggested that nudging could reduce errors at the expense of reducing variability, although Otte et al. (2012) found that nudging could improve predictions of both monthly means and hot and cold extremes of 2 m temperature. Feser (2006) emphasized the importance of scale separation when studying the impact of nudging. She used two dimensional digital low pass and band pass filters to study the standard deviation of 2 m temperature and sea level pressure, in order to demonstrate that the value of downscaling lies in the small scales where the regional scale or mesoscale model is able to contribute to the variance at scales that are not well resolved in the forcing data. Hahmann et al. (2014) used comparison with tall meteorological masts to show that frequent reinitialization, spectral nudging or grid nudging resulted in similar wind climate simulations over the sea, but they did not address the issue of wind speed variance. For wind resource assessment, reducing the variance of the wind speed at typical wind turbine hub-heights may impact estimates of the AEP, which relies on the full distribution of wind speed, or extreme winds, which rely on one tail of the distribution.

In this work, we conduct year-long simulations over the South Baltic region using the Weather Research and Forecasting (WRF) model with two nested domains with horizontal grid spacing of 15 km and 5 km respectively. A simulation reinitialized every 24 hours, with a spin-up period of 12 hours is treated as the 'control', and compared with simulations that are run with spectral or grid nudging applied to the 15 km domain. To ascertain any smoothing effect of the two nudging methods, temporal and spatial spectra of wind speed near the surface and at a height of 1150 m above ground level are used to show the frequency-dependent impact of the nudging on the two long experiments as compared with the short experiment. The detailed use of spatial and temporal spectra, and in particular maps of temporal spectra integrated over the mesoscale wavenumbers, brings a new angle to the analysis of nudging and the flow of information from the domain boundaries.

2. Experimental Setup

The three year-long simulations were run using the WRF model version 3.2.1 for 2010. Although wind climates are based on more than one year of data, this is a sensitivity study, for which a full annual cycle was considered sufficient. Two domains with horizontal grid spacing of 15 km and 5 km respectively (shown in Fig. 1) were used downscale the ERA Interim reanalysis (Dee et al. 2011), which has a spectral resolution of T255 (about 50 km at this latitude). The outer, 15 km domain had dimensions of 101 $\times$ 69 grid points, while the inner, 5 km domain had dimensions of 204 $\times$ 105 grid points.

Three configurations of the WRF model were tested. In the first configuration, the WRF model was re-initialized at 00 UTC for each day of 2010, and run for 36 hours in each case. By discarding a 12 hour spin-up time, the 24 hour time series starting at 12 UTC each day gave continuous coverage of the year. This simulation is referred to as the 'SHORT' model run (Table 1), and is considered the 'control' because there is no smoothing effect from the nudging, and because this is the typical method chosen for wind climate estimations (eg. Taylor et al. (2009)).

In the second configuration, the WRF model was re-initialized at 00 UTC every ten days, and run for 11 days in each case. Discarding a 24-hour spin-up time, the 10-day periods gave an analogous coverage to the short experiment. This simulation is labeled 'LONG-G' in Table 1. Grid point nudging (Skamarock et al. 2008) was used to constrain the large scale weather patterns in the 15 km resolution domain, while the 5 km nest was constrained only at the boundaries. Grid nudging was applied to the U and V wind components, potential temperature and water vapor mixing ratio for model level 11 (centered on $\sim$1150 m) up to the top of the model at 50 hPa, following the strategy of Rife et al. (2010). The grid nudging in the WRF model corrected the tendency term in the prognostic equation for each nudged variable with a weighted difference of the analysis field (in this case ERA-Interim) with the current value from the model, as described in Skamarock et al. (2008).

Results from Peña et al. (2013), who used modeling and ceilometer observations to construct a climatology of boundary layer heights at a Danish coastal site, suggest that model level 11 (1150 m) will almost always be above the top of the boundary layer in the regions considered in this study, which is important because the nudging should not suppress the development of mesoscale variability within the boundary layer. There is an alternative option in the WRF model to apply nudging only above the time-varying top of the boundary layer. However, due to concerns about nudging being applied close to the surface when the boundary layer height is small during stable conditions, this option was avoided. The nudging coefficient for all nudged fields was zero for levels 1–10, 3×10^{-5} s^{-1} at level 11, and 3×10^{-4} s^{-1} for level 12 to the top of the model at 50 hPa.

The third configuration of the WRF model (labeled 'LONG-S' in Table 1) was the same as the second, but spectral nudging was used instead of grid nudging. In spectral nudging, only wavelengths longer than a specified threshold are nudged. Nudging was applied to the

U and V wind components, potential temperature and geopotential for wavelengths longer than around 250 km in the zonal and meridional directions. The cut-off of 250 km was chosen after inspection of the average wind speed spectra of ERA-Interim over our study area as representing the information containing scales of the large scale forcing. This scale may in fact be too small, as discussed in section 5c.

Other than the nudging and length of the simulations, the three simulations used identical physical and dynamical settings. Vertical diffusion in the boundary layer was parametrized by the Mellor-Yamada-Janjic scheme, while the Janjic Eta scheme and the unified Noah land-surface model were applied to the surface layer and surface physics respectively. For sub-grid-scale convection, the Kain-Fritsch scheme was used on both domains, and microphysics was parametrized by the Thompson microphysics scheme. Shortwave and longwave radiation were calculated using the Dudhia scheme and the RRTM schemes respectively. The integrations on the two domains were executed simultaneously. One-way nesting was used so that spectral properties of the 15 km domain (to which nudging was applied) and the 5 km domain (to which nudging was not applied) could be studied independently. More details of the simulations and extensive validation against observational data can be found in Hahmann et al. (2014).

3. Observations

Measurement masts from 11 sites where wind speeds were measured at a height of at least 40 m with at least hourly resolution were used for validation. The stations include inland, coastal and offshore locations (Fig. 2). In cases where measurements at multiple heights were available, the wind speed at the height closest to 39 m was chosen for consistency with the height of the second model level. There was a measurement available within 9 m of 39 m at all sites except for Ryningsnäs, where the lowest measurement was at 98 m. Basic quality control was applied to remove wind speeds less than zero, segments with more than two repeated values and wind speeds greater than $30\,\mathrm{m\,s^{-1}}$ that are assumed to have been related to measurement errors. Since there were episodes of missing data in all the time series, all available data in the period January 2006 to December 2011 was used, rather than just the modeled study period of 2010 to increase the representativity of the data. This approach may have introduced differences in average variance due to inter-annual variation in large scale weather patterns in the region, although a comparison of the spectrum from the period 2006–2011 with that from only 2010 at Fino 1 (not shown) indicated little difference. The observed time series were split into 24-hour segments to calculate spectra. The number of 24 hour segments for each observation location, together with the percentage data coverage is given in Table 2. Note that this is not the overall data coverage, but the number of 24-hour periods that satisfied the quality control criteria.

4. Analysis of spectra and mesoscale variance

Spatial power spectra of the modeled wind speed were calculated as described in the Appendix for each west-east transect of the domain, and averaged over all such transects. Each west-east transect was detrended prior to calculating the power spectra. As described in the Appendix, a Hanning window was applied to each transect to alleviate end effects. In the temporal domain, the same procedure was used to calculate frequency spectra of 24 hour time series at each grid point.

The sum of the coefficients of the power spectrum is equal to the variance of the time series or spatial transect (e.g., Stull 1988, Chapter 8). To study the contribution to the variance from the mesoscale part of the spectrum, the scalar mesoscale variance, σ_m^2 is defined as the area under the power spectrum between the frequencies pertaining to the time scales of 2 and 8 hours (Eq. 1). The mesoscale wind speed variance, σ_m^2, which has units of $\mathrm{m^2\,s^{-2}}$, is defined as

$$\sigma_m^2 = \sum_{\frac{1}{T_2}<f<\frac{1}{T_1}} S(f)\Delta f, \tag{1}$$

where $T_1 = 2$ hours and $T_2 = 8$ hours, $S(f)$ is the power spectrum, f is the frequency, and Δf is the width of the frequency bins.

The spatial analogy of the mesoscale variance is

$$\sigma_{mk}^2 = \sum_{\frac{1}{x_2}<k<\frac{1}{x_1}} S(k)\Delta k, \tag{2}$$

where x_1 and x_2 are two length scales, $S(k)$ is the spatial power spectrum and k is the wavenumber. We chose x_1 and x_2 to be 72 and 288 km respectively, which relate to the temporal scales of 2–8 hours via a simplistic Taylor transformation with a nominal wind speed of $10\,\mathrm{m\,s^{-1}}$. The spatial propagation of atmospheric variability will be governed not only by the wind speed at the surface, but by the wind throughout the boundary layer (Larsén et al. 2013). Even though $10\,\mathrm{m\,s^{-1}}$ is higher than the mean wind speed over the land (see Fig. 4), it is representative of the wind speed at the top of the boundary layer.

5. Results

a. Spin-up periods of the three experiments

We compare the mean and mesoscale variance of the wind speed of the series of the SHORT simulation to that of the LONG-G and LONG-S simulations. We assume that the 11 day model runs, which are initialized every 10 days to create a continuous time series, are not affected by spin-up. Figure 3, showing the average spatial mesoscale variance, σ_{km} (Eq. 2) for each hour of the 36 hour and 11 day model runs at model level 2 (L2, centered at ∼39 m) and level 11 (L11, centered at ∼1150 m), suggests that this is a reasonable assumption, as the mesoscale variance appears to have settled into a steady diurnal oscillation after around 18 hours. For both the 5 km and 15 km domains, the mesoscale variance near the surface

(L2) is greater than that at L11. In the case of the SHORT runs, the maximum mesoscale variance at L11 is around 60% of that at the surface for both domains. For the LONG-S experiment, the mesoscale variance at L11 is around 55–60% of that at the surface for both domains, while for the LONG-G experiment it is around 33% and 55% of that at the surface for the 15 km and 5 km domains respectively. Note that both the short experiment and the long experiments are initialized at 00 UTC. The diurnal peak in mesoscale variance occurs, on average, at 18–19 UTC, which means that mesoscale variance appears to increase for the first 18 hours of the simulations. We do not explore the equivalent result for simulations initialized at 12 UTC, which may in fact under-represent the first diurnal peak in mesoscale variance after only 6–7 hours of simulation time, but Fig. 3 hints that the amount of spin-up required is dependent on the initialization time because of the prominent diurnal cycle in variance.

b. Average wind speeds

Hahmann et al. (2014) used the same modeling set-up to study the sensitivity of the simulated mean wind at 100 m in the WRF model to various parameters including choice of global reanalysis data, number of vertical levels, boundary layer parametrization and grid or spectral nudging. They found that the most important parameters for simulating mean wind speed at 100 m were the boundary layer parametrization and the length of spin-up period. Of particular relevance to this paper, they found that using grid or spectral nudging made differences of only ±1.5% in wind speed at 100 m, while frequently reinitializing the experiments without nudging made a difference only if an insufficient spin-up period was used.

Hahmann et al. (2014) also validated the long simulations against observations. They showed that the bias in mean wind speed was less than 3.6% at five offshore sites in the North and Baltic Seas with measurements from higher than 70 m above ground level. Poorer results were found for one offshore site that was in close proximity to a wind farm and located in the narrow channel between Denmark and Sweden. For an additional 5 onshore locations with measurements at heights between 30 and 125 m, there was a relative bias between -1.3 and 21.5%, with the worst result relating to a forested site.

This study focuses on the mesoscale variance in wind speed, which although related to the mean wind speed, requires a unique set of validation criteria and analysis techniques to those used in Hahmann et al. (2014). The average wind speed at L2 and L11 for one year of the SHORT simulations is shown in Fig. 4. These plots simply show the time-averaged model output, and should not be treated as input for wind resource assessment, as they are based on only one year of data and do not include microscale effects. In Fig. 5, the ratio of the mesoscale standard deviation (the square root of the mesoscale variance, as defined in Eq. 1) to the mean wind speed is shown. The plots show that the ratio of mesoscale wind standard deviation to mean wind speed is not constant in space. The highest ratio (up to 8%) is found over the complex topography in Norway and Sweden, where wind speeds are low due to the increased form drag of the topography, although the local wind speeds are often higher than those shown here due to microscale effects over the mountains. In general, the ratio is lower over the sea than over the land, but the ratio also varies between 4% and 7% even over apparently homogeneous areas of water such as the interior of the Baltic Sea, where there is little variation in mean wind speed (Fig. 4). Most of this spatial variation therefore comes from inhomogeneities in the mesoscale variance. This suggests that the mesoscale wind variance varies on a smaller length scale than the mean wind. Even at L11, there is variation in the ratio of standard deviation to mean wind of between 4% and 8% over the sea that is not reflected in the mean wind speed.

Although validation of the mean wind speed is of obvious importance, these results show that mesoscale wind variability should also be validated independently. This is important not only for end users of the model who may be interested in wind fluctuations, but for the scientific evaluation of mesoscale models, since the mesoscale scale variance reflects the extent to which mesoscale phenomena such as convective rolls, cellular convection, gravity waves or sea breezes are correctly simulated in the model.

c. *Average spectra in the temporal and spatial domains*

In this section, the scale-dependent differences in wind speed variability amongst the three experiments are explored using spatial and temporal spectra of the wind speed near the surface (L2) and the height at which the nudging is first active (L11). The aim of this analysis is to show which wavenumbers or frequencies are smoothed by the grid and spectral nudging. The advantage of the spatial spectra is that they include scales down to the smallest resolvable features in the model, and also allow us to examine the instantaneous spectra at various periods in the model initialization. Although the temporal spectra are calculated using 24-hour blocks, they allow us to uncover the spatial variation in the mesoscale wind variance, because a unique spectrum for every grid point can be calculated.

Spatial spectra were calculated along each row of the domains using the squared coefficients of the discrete Fourier transform (Eqs. A1 and A3 in the Appendix), and averaged to calculate a single spectrum. After subtracting the mean of each row, a Hanning window was applied to alleviate end-effects in the spectra (Eq. A2). The Hanning window had the added advantage of down-weighting the influence of the boundary regions on the average spectra, which are therefore most representative of conditions in the domain interior. Similar spectra were calculated along domain columns for comparison (not shown), and although there were small differences in the absolute values of the spectra, the relative differences among the experiments were nearly identical. The spectra show the average variance as a function of wavenumber and wavelength. The longest resolved wavelength is equal to the width of the domain, and the shortest resolved wavelength is the Nyquist criterion of $2\Delta x$, although the spectra may be subject to aliasing at the highest wavenumbers.

In Fig. 6, the average spatial spectra for the one year period are shown for L2 and L11, as well as the ratios between the LONG-G and LONG-S simulations with nudging on the outer nest, and the SHORT simulation (considered the control). The spectrum of the ERA

Interim wind speed fields that are interpolated onto the 15-km domain and used in the FDDA nudging algorithms is also indicated for comparison with the spectra at L11. Red curves are for the 5 km domain, to which nudging is not directly applied, and black curves are for the 15 km domain, to which nudging is applied at level 11 and upwards. In all plots, the thick dashed lines indicate spectral slopes of -3 and $-\frac{5}{3}$, as found in observational studies such as Nastrom and Gage (1985), and which are generally considered to delineate the synoptic scale variance from the mesoscale variance, as discussed in Skamarock (2004).

Figure 6 shows that at L2, the spectra for the three experiments are nearly identical. The spectra are not entirely smooth, but do not get smoother with increasing averaging periods (not shown), indicating that the irregularities in the spectra are most likely due to stationary topographic effects. The ratio of the variance from the LONG-G and LONG-S experiments to the SHORT experiment indicates that there are in fact some very small differences among the L2 spectra in the 15 km domain.

At L11, there is a clear difference among the spectra of the various experiments for the 15 km domain. The SHORT experiment has the highest variance, while the LONG-G experiment has the smallest spectral amplitude at all wavenumbers. The spectrum of the LONG-S experiment is similar to that of the LONG-G experiment for wavelengths longer than about 350 km, while for wavelengths shorter than about 180 km, it bears greater resemblance to the spectrum of the SHORT experiment. This is seen most clearly in the ratio of the spectra of the long simulations to that of the short simulations (Fig 6d), which for the spectral nudging case, return to a value close to unity for wavelengths shorter than about 180 km. This is the expected behavior, since the spectral nudging is applied for wavelengths longer than 250 km, which corresponds approximately to the minimum of the ratio of the spectra of the LONG-S experiments to that of the SHORT experiment for the 15 km domain. However, the fact that the spectrum of the LONG-S experiment begins to decrease in amplitude with that of the ERA-Interim before recovering suggests that the 250 km cut-off for the scale-dependent nudging may be too short. The ratios of the spectra (Fig 6d) show that at the longest wavelengths, the three experiments are nearly identical because all three are being dominated by long wavelengths that are forced from the boundaries and change relatively slowly. These wavelengths are captured well by all of the experiments. The variance of the LONG-S experiment is suppressed to around 60% of that in the SHORT experiment at a wavelength of around 280 km, then completely recovers to match the amplitude of the spectrum of the SHORT experiment for wavenumbers higher than about 180 km. For the LONG-G experiment, the variance drops in a similar manner to that in the LONG-S experiments, but it never recovers. The spectra for the LONG-G and LONG-S experiments follow the FDDA spectrum up to a wavelength of around 250 km, indicating the scales present in the subsection of the ERA Interim reanalysis data that are influencing the 15 km domain.

For the 5 km domain, the variance is also somewhat suppressed at L11 (Fig. 6d) for the experiments that have grid nudging or spectral nudging applied to the corresponding parent domain, but variance of the long experiments drops only to around 90% of that in the short experiment for the case of spectral nudging, and to around 80% of that in the short experiment in the case of grid nudging. The only connection between the 15 km domain and the 5 km domain is through the boundary region, suggesting that the larger gap in spectral amplitudes between the two domains imposed by the nudging is inhibiting the inner domain from developing the same degree of mesoscale variance as the short experiment without nudging.

In Fig. 7, analogous plots to those in Fig. 6 are shown, but for wind speed spectra in the temporal domain. The same methodology as for the spatial spectra described in the Appendix was used, but for spectra in the frequency domain instead of the wavenumber domain. For both the SHORT and the LONG experiments, a separate spectrum for each grid point and for each 24 hour period was calculated. For the SHORT experiment, this was hours 12–35 of each simulation, while for the long experiments, it was hours 36–59, 60–83, 84–107 etc. In this way, the same diurnal cycles were used for calculating the spectra of the long and short experiments. The time series were detrended and a Hanning window applied prior to calculating the spectra, analogous to the methodology for the spatial transects. Five grid points from the domain boundary were discarded when calculating the average spectra. The spectra show the average variance as a function of frequency and timescale. The spectra were calculated in blocks of 1 day, so the longest resolved timescale is 24 hours, and since the model output was saved hourly, the shortest timescale displayed in the figures is 2 hours, although aliasing may introduce errors into the spectra at this timescale. The spatial and temporal spectra may be related using an approximate Taylor transformation, where waves at the minimum of the ratio between the spectrally nudged and short experiment have a wavelength of 280 km (from Fig. 6) and a timescale of about 8 hours (from Fig. 7), using a nominal wind speed of $10\,\mathrm{m\,s^{-1}}$. The spectrum of the wind speed from the spectrally nudged experiments transitions to be closer to that of the short experiment at the highest frequencies, but never fully recovers the amplitude of the short experiment. The temporal spectra cover timescales longer than 2 hours, which using a nominal wind speed of $10\,\mathrm{m\,s^{-1}}$, relates to wavelengths greater than around 72 km on the spatial spectra.

Figure 8 shows the modeled and observed temporal wind speed spectra for the 11 validation sites that were described in section 3. The model spectra are a subset of those that were averaged over the whole domain in Fig. 7, chosen as the closest model grid points to the observational sites and vertically interpolated to match the heights of the observations. The observed time series were split into 24 hour segments, and the resolution of the observations was hourly. Segments with a single missing observation were filled using linear interpolation, while segments with more than one missing observation were rejected. A Hanning window was applied to both the observed and modeled time series. All WRF experiments show a spectral deficit relative to the observations, and the same relative differences between the long experiments with nudging and the short experiment without nudging as in Fig. 7 are seen.

Figure 9 shows the modeled mesoscale variance (Eq. 1) from the spectra in Fig. 8 for the 5 km domain against observed mesoscale variance for the 11 sites. Interestingly, we see that there is a positive correlation with $r^2 = 0.48$–0.56 for the three experiments, indicating that while the variance in the mesoscale model is too low, it may be reflecting realistic physical processes that differ between land and sea areas — for example, cellular convection over the sea, day-time convection over the land or sea breezes. The correlation for the SHORT experiment (0.56) is higher than that of the LONG-G and LONG-S experiments which both have a correlation of 0.48.

d. Maps of average temporal variability

Figure 9 indicates that the mesoscale variance varies between 0.15 and $0.35\,\mathrm{m^2\,s^{-2}}$ in the WRF simulations, and between 0.15 and $0.45\,\mathrm{m^2\,s^{-2}}$ in the observations. To further examine this variation, Eq. 1 is applied to every 24 hour period at every grid point, such that the scalar mesoscale variability can be mapped over the whole domain.

Figures 10 and 11 are maps of the time-averaged mesoscale wind speed variance for time scales of 2–8 hours, calculated for each 24 hour period of the year for the three experiments. The most obvious trend in all the plots is that the variance is higher over the sea than over the land at L2, consistent with Vincent et al. (2011) who showed higher mesoscale variability in flow from the sea than from the land at an offshore site in the North Sea west of Denmark, and Vincent et al. (2013) and Larsén et al. (2013) who studied the impact of cellular convection and gravity waves on the mesoscale part of the wind speed spectrum. This result is consistent with the observed spectra and mesoscale variance in Figs. 8 and 9. Furthermore, all experiments on both domains at L2 and L11 show reduced variance around the boundaries where the smoother fields are inherited from the boundaries.

For the 15 km domain (Fig. 10), the SHORT experiment has mesoscale wind speed variance of up to $0.2\,\mathrm{m^2\,s^{-2}}$ over the sea at L2, and up to $0.3\,\mathrm{m^2\,s^{-2}}$ over most of the interior of the domain at L11. At L11, the mesoscale variance is suppressed to less than $0.1\,\mathrm{m^2\,s^{-2}}$ in most areas for the LONG-G experiment, and less than $0.2\,\mathrm{m^2\,s^{-2}}$ for the LONG-S experiment. This reduction in variance relative to the SHORT experiment is expected, since L11 is the first level at which nudging is applied. On the other hand, the variance at L2 in the 15 km domain nudged experiments is also suppressed relative to the SHORT experiment, suggesting that the smoothing at L11 and above also propagates to the surface. Similar to L11, the mesoscale variance is suppressed more relative to that in the SHORT experiment in the LONG-G experiment than in the LONG-S experiment.

For the 5 km domain (Fig. 11), there is little impact of grid or spectral nudging of the 15 km domain at L2, but at L11 the variance is suppressed both over the Baltic Sea, where the short experiment has mesoscale variance of around $0.4\,\mathrm{m}^2\,\mathrm{s}^{-2}$ and both experiments with nudging have variance as low as $0.3\,\mathrm{m}^2\,\mathrm{s}^{-2}$, and over the land, particularly over the complex topography in Sweden. Despite there being no nudging applied to the 5 km experiments, the smoothing caused by the nudging of the 15 km domain has propagated into the inner nest.

6. Discussion

The wind speed spectra for the 15 km domain for the short experiment initialized every 24 hours, and the long experiments initialized every 10 days with either grid or spectral nudging demonstrate that the nudging results in a smoothing of the simulated wind speeds. In particular, grid nudging causes suppressed variance at all wave numbers, including those beyond the effective resolution of the ERA-Interim reanalysis towards which the simulations are nudged. In contrast, spectral nudging results in a wind speed spectrum with suppressed variance at the wavenumbers for which the nudging is specified, which then transitions to a spectrum similar to that of the short experiment for higher wave numbers (Figs. 6 and 7).

Both the spatial and temporal spectra for the 5 km domain transition to a shallower spectral slope in the mesoscale part of the spectrum than that in the sub-mesoscale range, with the transition occurring at around 320 km for the spatial spectra and around 14 hours for the temporal spectra (Figs. 6 and 7). However, neither spectrum attains the spectral slope of $-\frac{5}{3}$ that is usually observed in the mesoscale range (e.g., Larsén et al. 2013; Nastrom and Gage 1985)). There is no noticeable difference between the 5 km simulations nested in the three alternative versions of the outer domain, either in the position of the transition or in any of the average spectral amplitudes. For the 15 km domain, the long simulations with grid and spectral nudging have less variance than the short simulations, and at the observation locations, all three experiments on both domains have less variance than the observed spectra.

There are some important differences between the spatial and temporal spectra, particularly at L2, where an influence of the nudging is still seen in the 15 km domain in the temporal spectra but is almost absent in the spatial spectra. The apparent differential impact of the nudging on the spatial and temporal spectra may be due to the fact that the spectrum of the spatial wind field can be strongly influenced by stationary topographic effects that develop quickly in the model, such as the acceleration of the wind over hills, or adjustments of the wind profile due to surface roughness changes. The temporal spectra may be more subject to slowly developing mesoscale features, particularly over the sea, such as cellular convection and sea breeze circulations that could be more sensitive to nudging. This is an interesting difference between the spatial and temporal spectra, and points to a potential limitation of using spatial spectra to study the variability in mesoscale processes near the surface.

The maps of mesoscale variance for the 15 km domain (Fig. 10) show that mesoscale variance is suppressed in the two experiments with nudging relative to the SHORT experiment. Averaged over the whole domain and whole simulation period, the mesoscale variance is reduced by 26% at L2 and 64% at L11 in the LONG-G experiments when compared with the SHORT experiment, and by 16% at L2 and 38% at L11 in the LONG-S experiments. Although the correct spatial distribution of mesoscale variance is unknown, the comparison with observations suggests that it is underestimated in all the experiments presented here. The differences in mesoscale variance between the short experiment and the long experiments with nudging suggest a smoothing effect of the nudging, even at the surface where the nudging is not applied directly. The difference is greater over the sea, suggesting that the nudging might inhibit the development of organized mesoscale structures such as convective rolls or cellular convection that are typically found over the water.

The simulations on the 5 km domain do not have nudging applied directly, but inherit some impacts of the nudging from the 15 km domain. Despite the fact that the three 5 km domain experiments are identically allowed to spin-up mesoscale variance in the domain interior, the maps of mesoscale variance for the 5 km simulations (Fig. 11) indicate that there are some persistent and systematic differences amongst the three experiments. Even though the actual boundary forcing is only applied to a frame 5 grid points wide around the edge of the domain, the region of suppressed variance persists for up to 200 km from the edge of the domain in the SHORT experiment, particularly at the western side which is the dominant inflow boundary. Vincent et al. (2013) suggested that open cellular convection was a dominant driver of mesoscale variability over the North Sea, and showed that cells took 5–6 hours to develop in idealized simulations with the WRF model. With a nominal wind speed of $10\,\mathrm{m\,s^{-1}}$, this time corresponds to a distance of 180 km, or around 3 degrees in longitude. This is consistent with the distance affected by reduced variance in all three experiments, a result that could inform decisions about choice of domain size, particularly where the boundary region is influenced by flow over large water bodies where mesoscale phenomena tend to dominate.

The maps of integrated mesoscale temporal variance offer a unique perspective of showing the spatial patterns in how information is shared between simulations and their respective parent domains. In particular, the extent to which the variance is suppressed around the boundaries of the domains, and the difference in variance between the land and the sea would be impossible to see using spatial spectra alone.

Figure 6 shows that the spectrum of the experiments with spectral nudging is nearly identical to that of the grid nudging spectrum at low wavenumbers, then transitions to a spectrum that is more similar to that of the short experiment at the highest wave numbers.

At the lowest wavenumbers, the spectrum of the short experiment is also close to that from the large scale forcing, but at the highest wavenumbers, the short spectrum reflects the fact that the mesoscale model has spun-up more variance than was in the large scale forcing. Around this transition region, there is a minimum in the ratio of the spectrum of the spectral nudged simulations to that of the short simulations. This reflects the large gap between the effective resolution of the ERA-Interim Reanalysis (which has an equivalent horizontal grid spacing of 50 km) and the outer domain with dx = 15 km. Ideally, this transition should take place in the part of the spectrum where the spectrum of the mesoscale models is still close to that of the large scale forcing. In our case, the spectral nudging is applied for wavenumbers longer than 250 km, which nearly matches the position of maximum deficit between the spectrum of the spectral nudged experiments and that of the short experiment: 250-300 km on the spatial spectra, or around 8 hours on the temporal spectra.

Verification of the spatial patterns in mesoscale variance is challenging because of the of the limited availability of observations. However, the scatter plot of modeled against observed variance at 11 observational sites in Fig. 9, suggests that while the mesoscale variance is suppressed in all experiments, there may be some skill in the model that could be enhanced using statistical modeling to produce maps of realistic levels of mesoscale variance, at least up to the time scale of 2 hours considered here. Fig. 9 indicates that the pronounced differences between mesoscale variance over the land and over sea that are seen in the model are probably realistic. While it can be argued that turbulence is greater over the land than over the water due to the enhanced surface roughness, the spatial and temporal scales we are studying here are considerably longer than those of turbulence. In fact, it has been shown that greater hour-scale fluctuations may be found over the water. For example, Larsén et al. (2013) demonstrated that the power spectrum at the Horns Rev wind farm in the North Sea showed greater amplitude during cases of open cellular convection than the climatological mean, and Vincent et al. (2013) showed that such phenomena can introduce large hour-scale fluctuations into the wind speed. Mesoscale phenomena such as open and closed cellular convection, convective rolls and gravity waves are unlikely to retain their regular, periodic structure when they are advected over the topography and various surface effects over the land, so may be a source of differential mesoscale variance between the water and the land.

7. Conclusions

In this study, spatial and temporal spectra were used to compare the mesoscale variability in regional climate simulations with daily initialization, grid nudging and spectral nudging. In agreement with other studies, it was found that grid nudging results in a smoothing at all wavelengths, while spectral nudging mainly affects longer wavelengths. Integrating temporal spectra over the wavenumbers of interest resolves the horizontal variation in the impacts of the boundary conditions and grid and spectral nudging. This approach showed that the nudging applied at L11 and above also causes smoothing at the surface. On an inner nest with no nudging, there was little impact of nudging the parent domain at the surface. At L11, reduced variance around the domain boundaries relative to the equivalent experiments nested in an outer domain without nudging suggested that some smoothing was inherited from the parent domain. This smoothing at the boundaries due to enforcement of the boundary conditions persisted for up to 200 km inward from the boundary dominant inflow boundary. The results indicated that when using spectral nudging in the external domain, the interior domain is able to generate more mesoscale variability in wind speed than when using grid nudging, even though the choice of nudging method has little effect on the mean wind speed as shown in Hahmann et al. (2014).

Although nudging is usually used to improve the representation of the mean flow, it also has an impact on the amount of variance for wavelengths that are not resolved in the large scale forcing. For areas such as wind energy, the hour-scale variability could be important, either for the spread of the wind speed distribution which is required for calculating the annual energy production, or for assessing the nature of hour-scale power fluctuations which may be correlated over a large area. Furthermore, there could be a small up-scale transfer impact, if mesoscale variability is suppressed and consequently impacts larger scales. We note that increased variance cannot necessarily be equated with improved skill, since we do not determine when (in the case of the average temporal spectra) or where (in the case of the average spatial spectra) the increased variability occurs.

The analysis here was limited to single choice of nested domains. Interestingly, since the 5 km domain appeared to inherit reduced variance from the boundaries of the 15 km domain when grid or spectral nudging was applied, the positioning of the nests will influence the mesoscale variance in the inner domain. Further experiments are required to explore this aspect of the nudging. However, it may be more likely to see an adverse effect of the nudging if the boundaries of the nest are placed in regions that are particularly favorable for the development of mesoscale variability, such as in the North Sea region, where mesoscale phenomena such as cellular convection are frequently observed. The results here also relate to a single choice of nudging coefficient. The degree of smoothing and the impact on model bias has been shown to be related to the nudging coefficient (eg. Bowden et al. (2012), Bullock et al. (2014)), and the relationship between the nudging coefficient and the reduction in mesoscale variance is an interesting area for further study.

The analysis of the spatial and temporal spectra reflected the same trends, but are not identical. This is partly because the spatial spectra are influenced by stationary topographic effects (since we consider the wind speed at an approximately constant height above ground level), and partly because the Taylor hypothesis will not apply in all cases at the wavelengths that we consider. For the spatial spectra, two-dimensional longitudinal spectra were used, but very similar results were obtained from the equivalent lateral spectra. The maps of mesoscale variability have applications beyond those used here, for example in studying the impact of observation based initialized strategies such as variational assimilation or observation nudging on the evolution and maintenance of mesoscale variability.

The results suggest that running the model for 10-day periods without re-initialization and with grid or spectral nudging applied to an outer nest is a reasonable configuration for nested regional climate simulations that is comparable to short runs with daily re-initialization discarding the first 12 h, although care should be taken near the edges of the domain. The long-reinitialization method saves considerable computer resources and results in time series that are more consistent with each other.

Acknowledgments.

This work was supported by the Danish Council for Independent Research – Technology and Production Sciences (case number 10-093196) individual post-doc project and the EU projects 'NORSEWind' (contract TREN-FP7-219048) and 'South Baltic Offer - South Baltic Offshore Wind Energy Regions' (contract WTPB.02.02.00-56-004/09). We would like to thank Dong energy, Vattenfall and the German Federal Environment Ministry (BMU) for sharing many of the observations used in the study, and Anna Rutgersson (Uppsala University) for making the Östergarnsholm data available. Thanks to Sven-Erik Gryning (DTU Wind Energy) for helpful comments on the manuscript.

APPENDIX

Calculation of the spatial power spectrum

The coefficients of the discrete Fourier transform, $A(k)$, were calculated according to

$$A(k) = \sum_{j=0}^{N-1} \left(U(j) - \bar{U}\right) W(j) e^{-2kj\mathrm{i}/N}, \tag{A1}$$

where U is the wind speed along a transect of the domain, j is the index of the gridpoint, W is the window function, k is the wavenumber, $\mathrm{i} = \sqrt{-1}$ and N is the length of U (e.g. Welch 1967). In our case, a Hanning window (e.g. Oppenheim and Schafer 2009, pp. 468) is used, defined as

$$W(j) = 0.5 \left[1 - \cos\left(\frac{2\pi j}{N-1}\right)\right]. \tag{A2}$$

The power spectrum, $S(k)$ is then calculated as

$$S(k) = \frac{2}{C_w N f_s} |A(k)|^2, \qquad 0 \leq k \leq \tfrac{N}{2}, \tag{A3}$$

where C_w is a correction due to the window function (e.g. Welch 1967),

$$C_w = \frac{1}{N} \sum_{j=0}^{N-1} W^2(j), \tag{A4}$$

and f_s is the sampling resolution, in this case equal to $\frac{1}{dx}$, where dx is the horizontal grid spacing.

REFERENCES

Bowden, J. H., C. G. Nolte, and T. L. Otte, 2013: Simulating the impact of the large-scale circulation on the 2-m temperature and precipitation climatology. *Clim. Dyn.*, **40**, 1903–1920.

Bowden, J. H., T. L. Otte, C. G. Nolte, and M. J. Otte, 2012: Examining interior grid nudging techniques using two-way nesting in the WRF model for regional climate modeling. *J. Clim.*, **25 (8)**, 2805–2823.

Bullock, O. R., K. Alapaty, J. A. Herwehe, M. S. Mallard, T. L. Otte, R. C. Gilliam, and C. G. Nolte, 2014: An observation-based investigation of nudging in WRF for downscaling surface climate information to 12-km grid spacing. *J. Appl. Meteorol. Climatol.*, **53**, 20–33.

Dee, D. P., et al., 2011: The ERA-Interim reanalysis: configuration and performance of the data assimilation system. *Q. J. R. Meteorol. Soc.*, **137**, 553–597.

Feser, F., 2006: Enhanced detectability of added value in limited-area model results separated into different spatial scales. *Mon. Wea. Rev.*, **134**, 2180–2190.

Hahmann, A. N., C. L. Vincent, A. Peña, J. Lange, and C. B. Hasager, 2014: Wind climate estimation using WRF model output: method and model sensitivities over the sea. *Int. J. of Climatol.*, doi:10.1002/joc.4217.

Larsén, X. G., C. Vincent, and S. Larsen, 2013: Spectral structure of mesoscale winds over the water. *Q. J. R. Meteorol. Soc.*, **139**, 685–700.

Liu, P., A. P. Tsimpidi, Y. Hu, B. Stone, A. G. Russell, and A. Nenes, 2012: Differences between downscaling with spectral and grid nudging using WRF. *Atmos. Chem. Phys.*, **12 (8)**, 3601–3610.

Lo, J. C.-F., Z.-L. Yang, and R. A. Pielke, 2008: Assessment of three dynamical climate downscaling methods using the Weather Research and Forecasting (WRF) model. *J. Geophys. Res.*, **113**, 1–16.

Miguez-Macho, G., G. L. Stenchikov, and A. Robock, 2004: Spectral nudging to eliminate the effects of domain position and geometry in regional climate model simulations. *J. Geophys. Res.*, **109**, 1–15.

Nastrom, G. D. and K. S. Gage, 1985: A climatology of atmospheric wavenumber spectra of wind and temperature observed by commercial aircraft. *J. Atmos. Sci.*, **42**, 950–960.

Oppenheim, A. V. and R. W. Schafer, 2009: *Discrete-Time Signal Processing*. 3d ed., Prentice Hall, Upper Saddle River, NJ, USA, 1120 pp.

Otte, T. L., C. G. Nolte, M. J. Otte, and J. H. Bowden, 2012: Does nudging squelch the extremes in regional climate modeling? *J. Clim.*, **25**, 7046–7066.

Peña, A., S.-E. Gryning, and A. N. Hahmann, 2013: Observations of the atmospheric boundary layer height under marine upstream flow conditions at a coastal site. *J. Geophys. R.*, **118**, 1924–1940.

Rife, D., J. Pinto, A. Monaghan, C. Davis, and J. Hannan, 2010: Global distribution and characteristics of diurnally varying low-level jets. *JOC*, **23**, 5041–5064.

Skamarock, W. C., 2004: Evaluating mesoscale NWP models using kinetic energy spectra. *Mon. Wea. Rev.*, **132 (12)**, 3019–3032.

Skamarock, W. C., et al., 2008: A Description of the Advanced Research WRF Version 3. Technical report NCAR/TN475+STR. Tech. Rep. June, NCAR, 113 pp.

Sørensen, P., N. A. Cutululis, A. Vigueras-Rodríguez, H. Madsen, P. Pinson, L. Jensen, J. Hjerrild, and M. Donovan, 2008: Modelling of power fluctuations from large offshore wind farms. *Wind Energy*, **11**, 29–43.

Stull, R. B., 1988: *An Introduction to Boundary Layer Meteorology*, Atmospheric and Oceanographic Sciences Library, Vol. 13. Springer, 680 pp., iSSN 978-90-277-2769-5.

Taylor, M., J. Freedman, and K. Waight, 2009: Using simulated wind data from a mesoscale model in MCP. Tech. rep., AWS Truewind.

Vigueras-Rodrìguez, A., P. Sørensen, N. A. Cutululis, A. Viedma, and M. H. Donovan, 2010: Wind model for low frequency power fluctuations in offshore wind farms. *Wind Energy*, **13**, 471–482, doi:10.1002/we.368.

Vincent, C. L., X. G. Larsén, S. E. Larsen, and P. Sørensen, 2013: Cross-spectra over the sea from observations and mesoscale modelling. *Boundary-Layer Meteorol.*, **146 (2)**, 297–318.

Vincent, C. L., P. Pinson, and G. Giebel, 2011: Wind fluctuations over the North Sea. *Int. J. Climatol.*, **31**, 1584–1595.

Welch, P. D., 1967: The use of fast Fourier transform for the estimation of power spectra: A method based on time averaging over short, modified periodograms. *IEEE Transactions on Audio and Electroacoustics*, **15 (2)**, 70–73.

List of Tables

Table 1. Description of the experiments

Experiment name	Simulation length	Spin-up length	Nudging type
SHORT (control)	36 hours	12 hours	none
LONG-G	11 days	24 hours	grid nudging
LONG-S	11 days	24 hours	spectral nudging

TABLE 2. Data availability for the 11 observation verification sites. C: Coastal sites. L: Land sites. S: Offshore sites.

Station Name	Data availability (DD/MM/YYYY)	N included days	% days covered	Height [m]
Høvsøre (HV) (C)	01/01/2006–31/12/2011	1906	87	40
Østerild W (OW) (L)	15/04/2010–11/09/2011	445	87	44
Ryningsnäs (RY) (L)	18/11/2010–31/12/2011	350	86	98
FINO1 (F1) (S)	01/01/2006–31/12/2011	1826	83	40
FINO2 (F2) (S)	01/08/2007–31/12/2011	1160	72	40
Lillegrund (LG) (S)	01/01/2009–31/12/2009	291	80	40
Horns Rev 1 (HR1) (S)	01/01/2004–15/12/2009	973	45	40
Horns Rev 2 (HR2) (S)	25/06/2009–19/08/2011	257	32	40
Tystofte (TY) (L)	30/05/2006–31/12/2011	1572	77	39
Östergarnsholm (OG) (C)	28/06/2006–20/10/2009	745	62	30
Risø (RI) (L)	01/01/2006–31/12/2011	1461	67	44

List of Figures

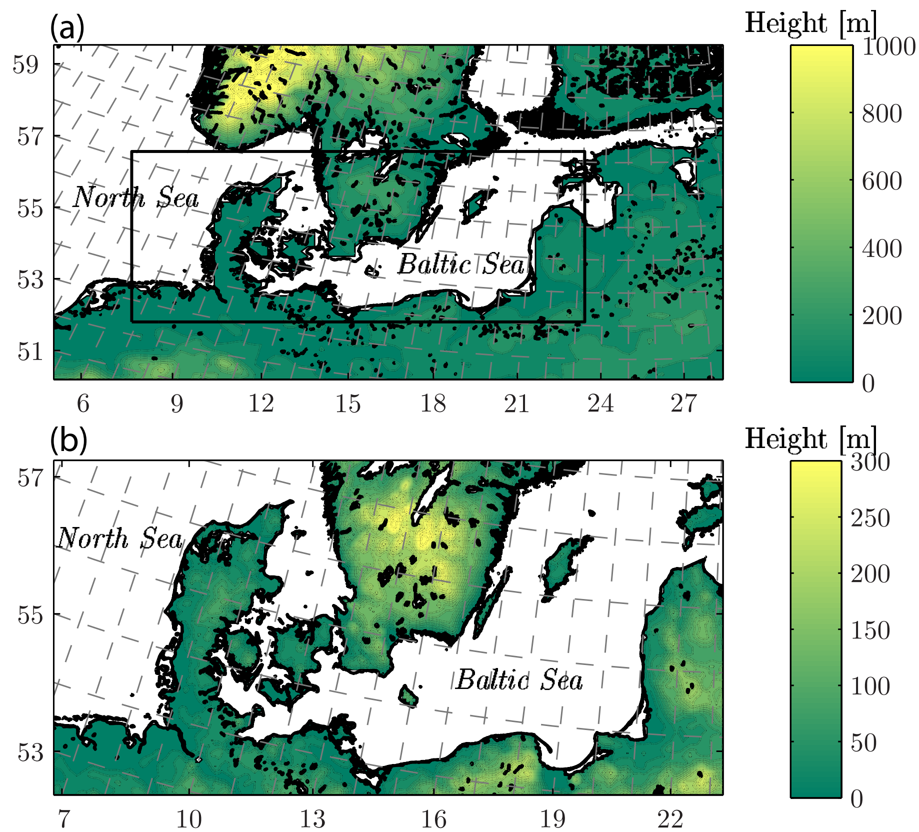

FIG. 1. Topography maps for the 15 km (a) and 5 km (b) domains. The boundaries of the 5 km nest are indicated as a black line in (a).

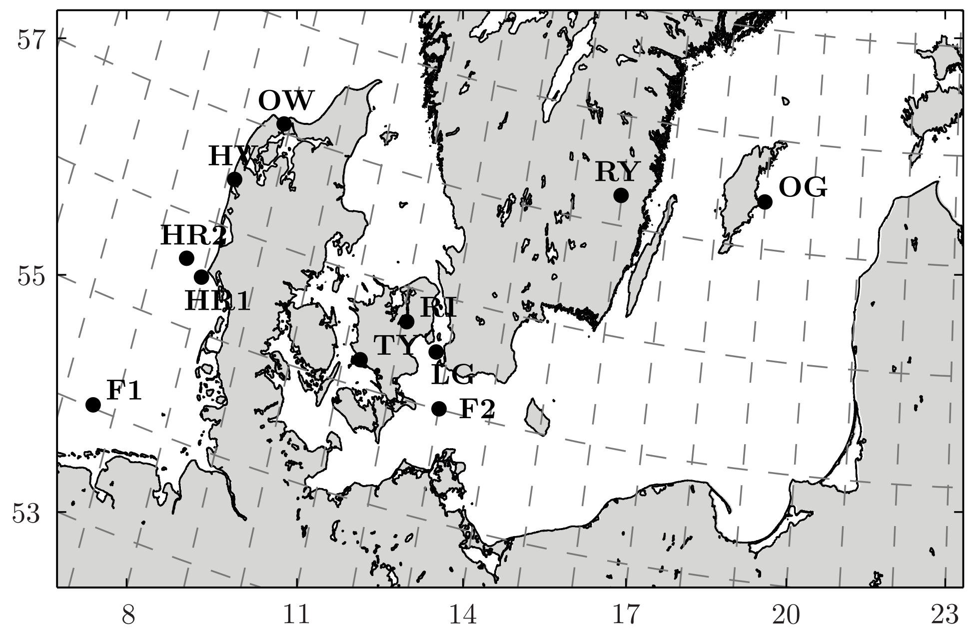

FIG. 2. The 11 observation sites used for verification of the modeled temporal spectra.

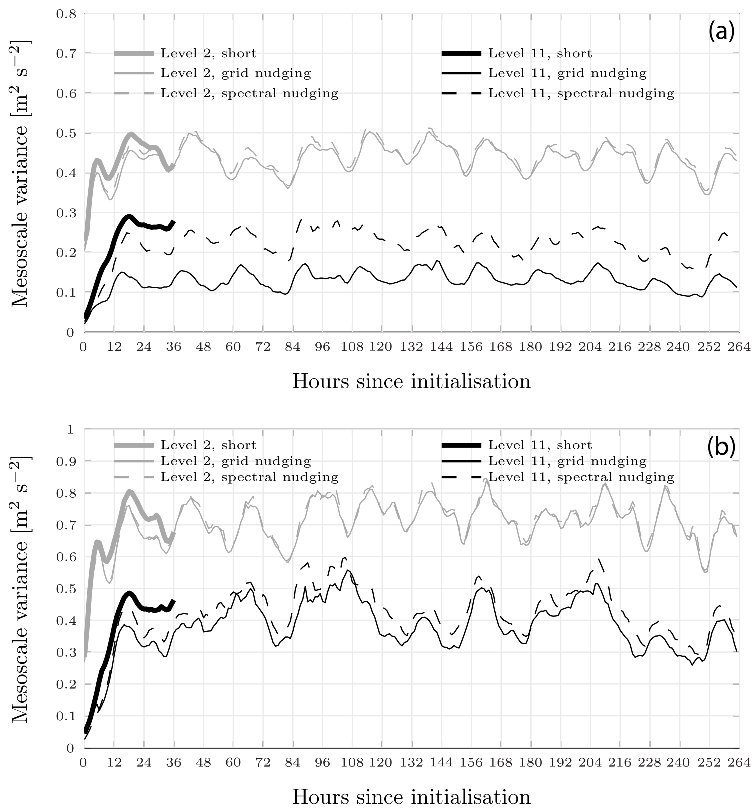

FIG. 3. Domain-average mesoscale variance (σ^2_{mk}) for each hour after simulation initialization for the (a) 15 km (outer) domain and the (b) 5 km (inner) domain. Simulations are averaged over a 1-year period.

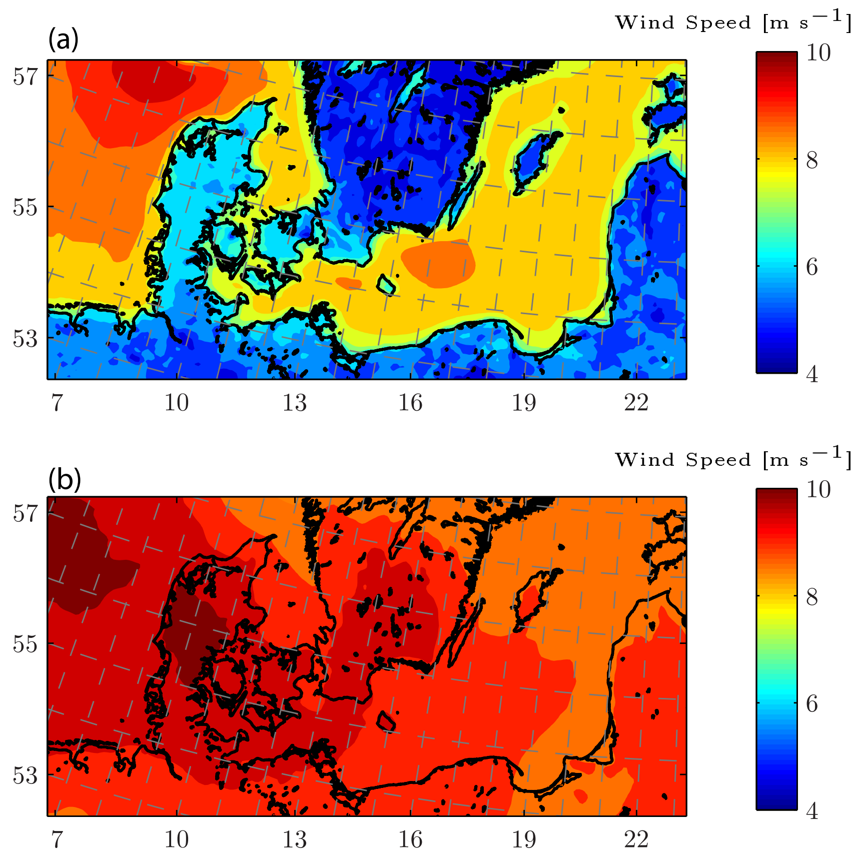

FIG. 4. Mean wind speed at (a) L2 and (b) L11 for the 5 km (inner) domain of the SHORT simulation for the 1-year test period.

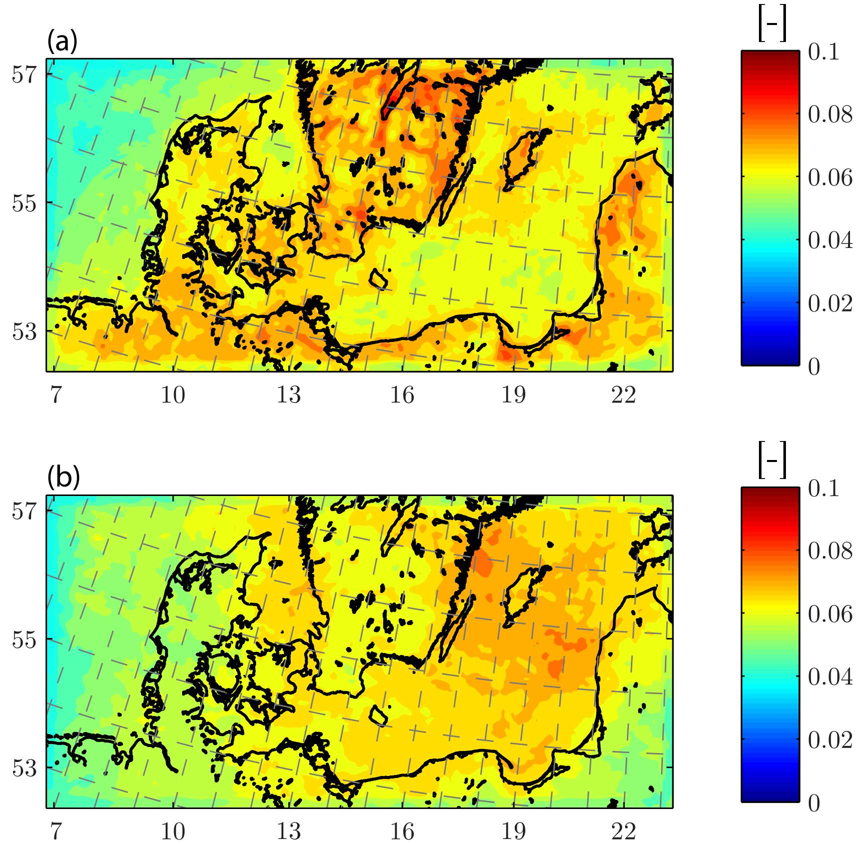

FIG. 5. The ratio of the mesoscale standard deviation to the mean wind speed at (a) L2 and (b) L11 for the 5 km (inner) domain of the SHORT simulation for the 1-year test period.

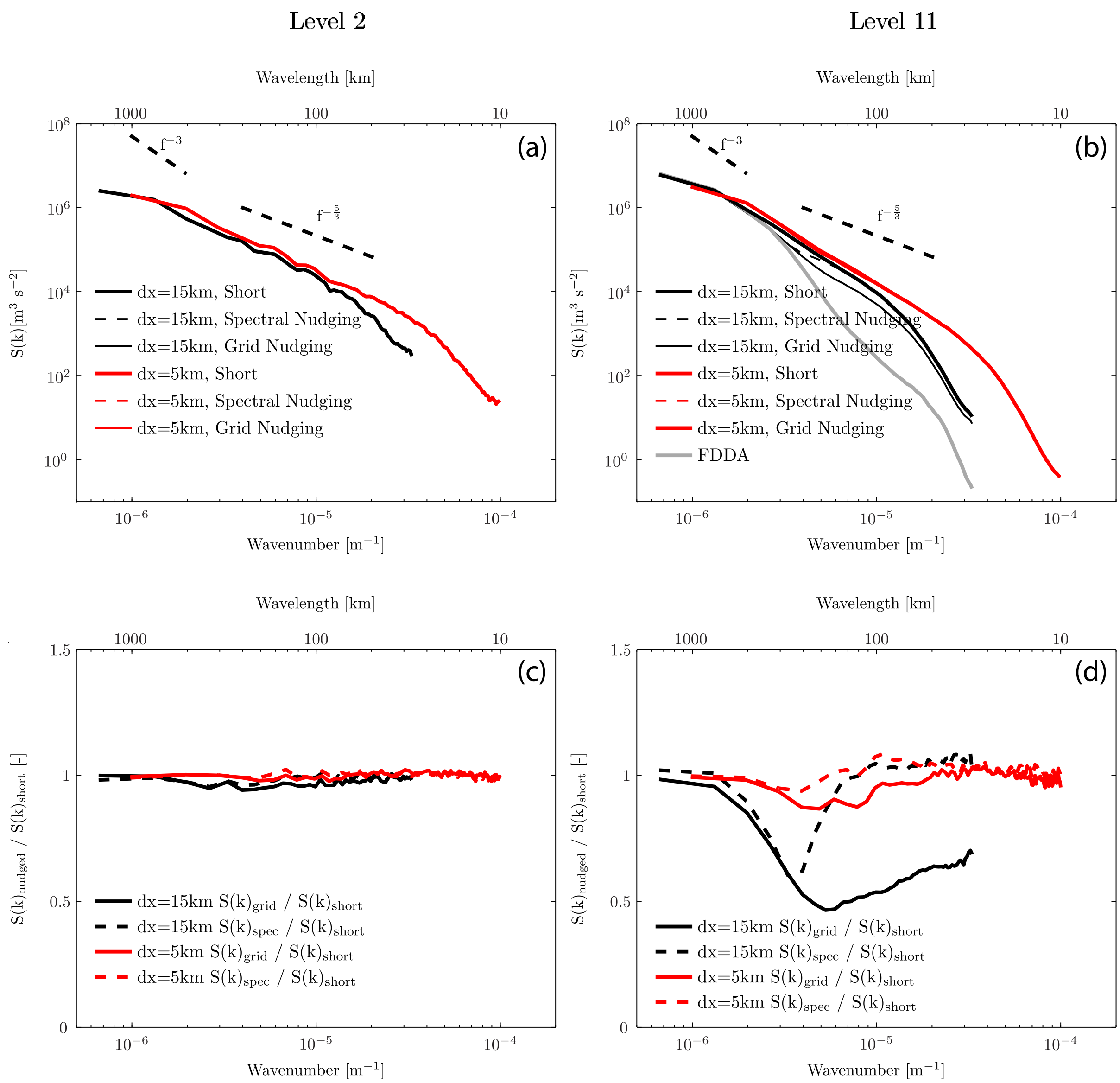

FIG. 6. Spatial wind speed spectra for L2 (a) and L11 (b) averaged over a 1-year period. Thick lines: SHORT experiment; Thin lines: LONG-G experiments; Dashed lines: LONG-S experiments; Thick grey line: FDDA input. The dashed line indicates slopes of -3 and $-\frac{5}{3}$. Ratio of the spatial wind speed spectra of the LONG-G experiments (solid) and LONG-S (dashed) to the wind speed spectra of the SHORT experiment for L2 (c) and L11 (d). The red curves relate to the 5 km domain and the black curves relate to the 15 km domain.

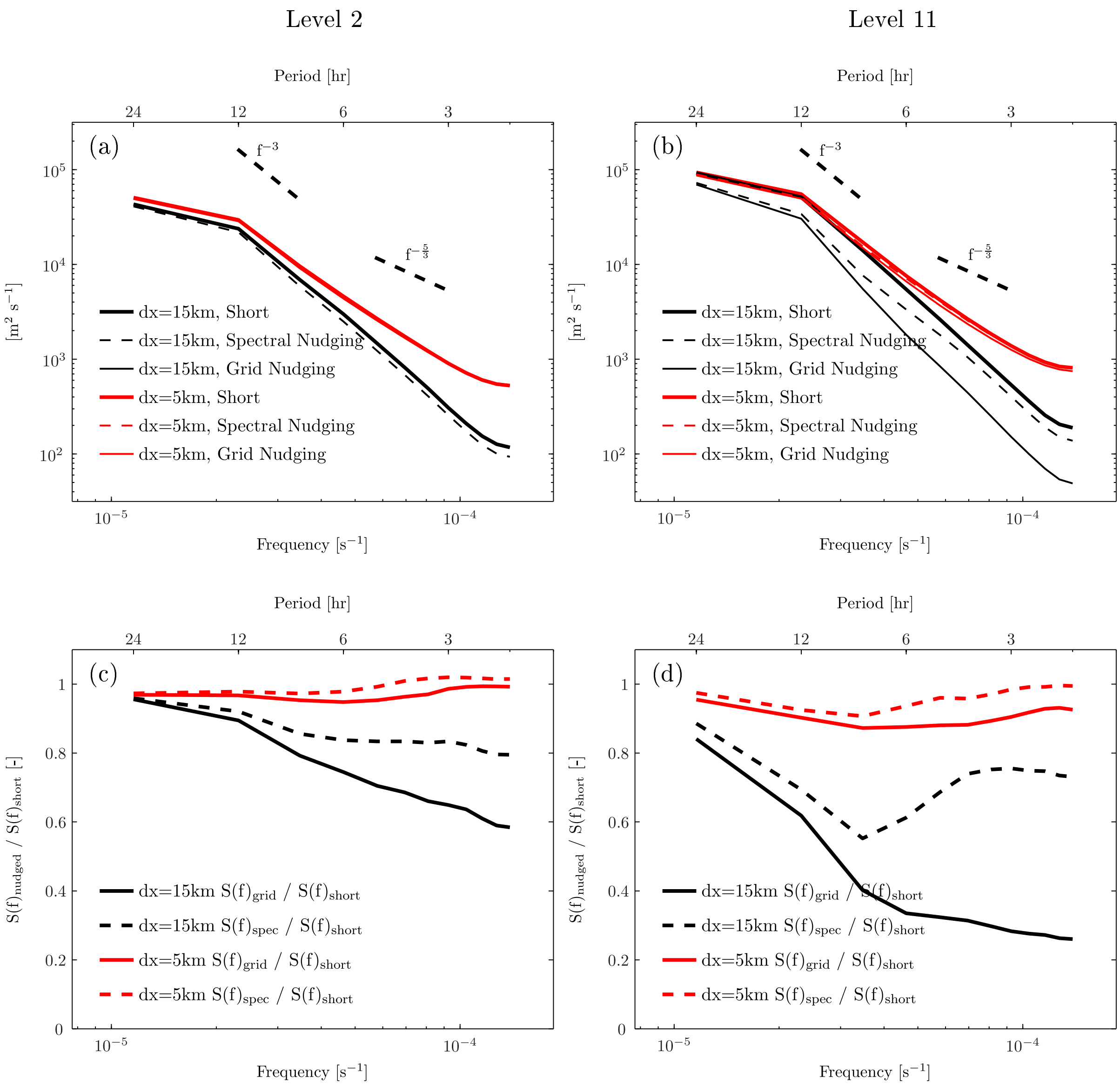

FIG. 7. As in Fig. 6, but for the temporal spectra.

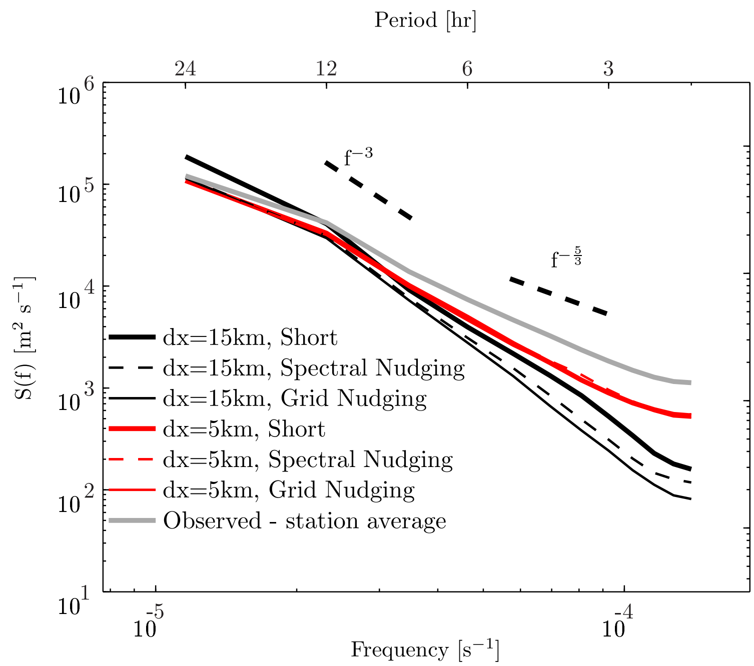

FIG. 8. Average temporal wind speed spectra for the 11 observation sites for the 5 km domain (red) and the 15 km domain (black). The observed average spectrum is shown in grey and the line styles as in Figs. 6 and 7.

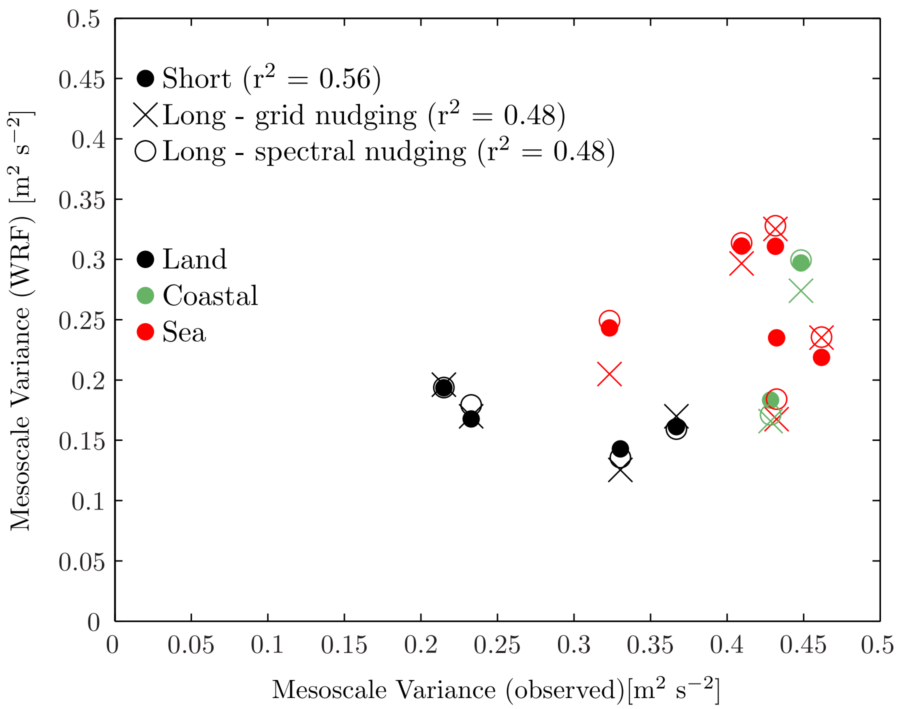

FIG. 9. Average modeled mesoscale variance of wind speed (5 km domain) against averaged observed mesoscale variance for the 11 observation sites for the SHORT, LONG-G and LONG-S experiments. Coastal, land and offshore sites are indicated by the green, black and red markers respectively.

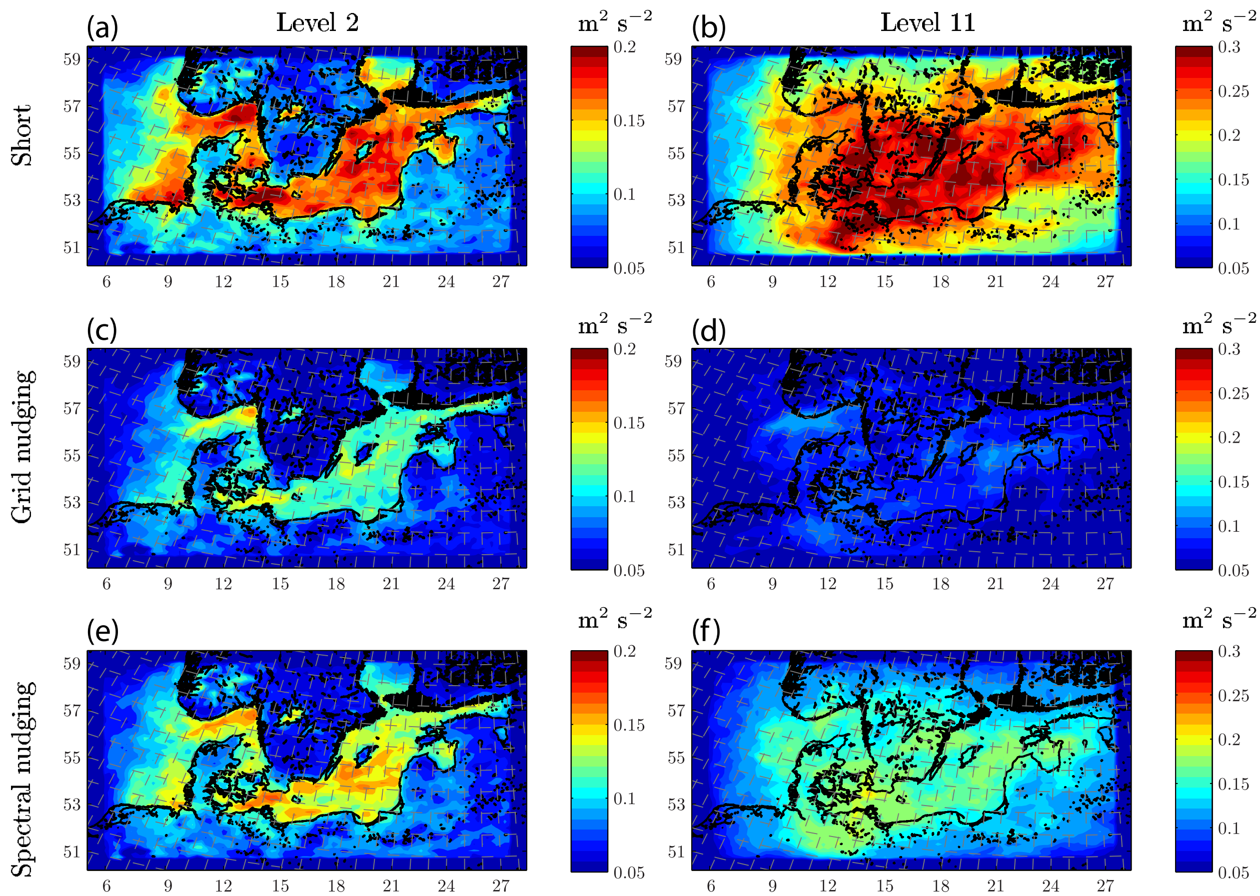

FIG. 10. Mesoscale variance of wind speed ($\mathrm{m^2\,s^{-2}}$) averaged over a 1-year period from temporal spectra for time scales of 2–8 hours for the 15 km domain for the SHORT (a and b), LONG-G (c and d) LONG-S (e and f) experiments at L2 (left) and L11 (right).

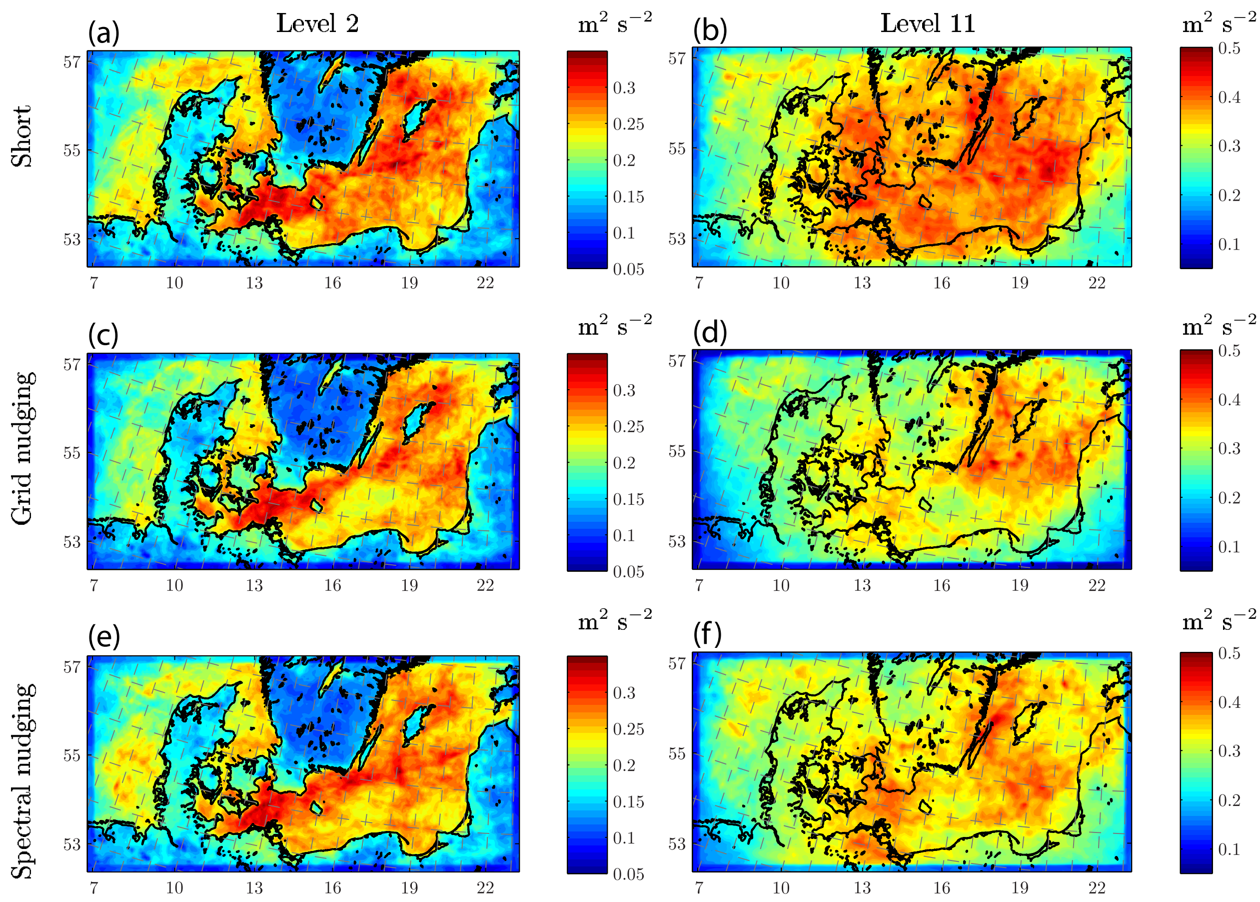

FIG. 11. Same as figure 10, but for 5 km domain.